Artificial Organs

Artificial Organs
35(2):145–156, Wiley Periodicals, Inc.

A Strain-Based Flow-Induced Hemolysis Prediction Model Calibrated by In Vitro Erythrocyte Deformation Measurements

Yangsheng Chen and M. Keith Sharp

Department of Mechanical Engineering, University of Louisville, Louisville, KY, USA

Abstract: Hemolysis is caused by fluid stresses in flows within hypodermic needles, blood pumps, artificial hearts, and other cardiovascular devices. Developers of cardiovascular devices may expend considerable time and effort in testing of prototypes, because there is currently insufficient understanding of how flow-induced cell damage occurs to accurately predict hemolysis. The objective of this project was to measure cell deformation in response to a range of flow conditions, and to develop a constitutive model correlating cell damage to fluid stresses. An experimental system was constructed to create Poiseuille flow under a microscope with velocities up to 4 m/s, Reynolds number to 200, and fluid stresses to 5000 dyn/cm^2. Pulsed laser illumination and a digital camera captured images of cells deformed by the flow. Equilibrium equations were developed to relate fluid stresses to cell membrane tension, and a viscoelastic membrane model was used to predict cell strain. Measurements of aspect ratio as a function of shear stress and duration of shear were used to calibrate the cell deformation model. Hemolysis prediction was incorporated with a threshold strain value for cell rupture. The new model provides an improved match to experimentally observed hemolytic stress thresholds, particularly at long exposure times, and may reduce the empiricism of hemolysis prediction. **Key Words:** Blood—Red blood cell—Blood damage—Shear stress—Microscope image.

Hemolysis is defined as the release of hemoglobin into plasma due to damage to erythrocyte membranes. Lokhandwalla and Sturtevant (1) categorized the factors causing cell lysis to be thermal/radiation, mechanical, and chemical. Mechanical lysis, the focus of this study, can be caused by fluid stresses in flows within hypodermic needles (2), blood pumps (3), ventricular assist (4), and other cardiovascular devices; can be induced in stenotic restrictions in the native circulation (5); and can be severe in incompletely closed patent ductus arteriosus (6,7). Hemolysis can impact laboratory test results by products liberated from the cells, or by interfering with certain assays. Hemolysis can also cause pain and discomfort during dialysis sessions (8), and extreme hemolysis is toxic, resulting in renal dysfunction and other organ failure. Considerable time and effort may be expended in testing prototypes of cardiovascular devices to avoid such problems, because insufficient understanding currently exists on how flow-induced cell damage occurs to accurately predict hemolysis.

Erythrocytes exhibit a number of patterns of deformation under different flow conditions. As shear rate increases in pure shear flow, cell shape changes from biconcave disk to ellipsoid, then to an elongated spindle-like shape with long axis approximately aligned with the flow (9,10). Viscosities of the internal and external phases of the RBC also influence rheologic behavior. Observation with a rheoscope (11) demonstrated that: (i) for low external phase viscosity, cells tended to tumble and behave unstably in the shear field; (ii) above a critical level of external phase viscosity, cells became stably oriented and elongated in the direction of shear; (iii) when stable orientation was achieved, the cell membrane rotated about the cytoplasm (tank-treading), with both deformation and frequency of rotation increasing with shear rate; (iv) at constant shear rate, RBC deformation

doi:10.1111/j.1525-1594.2010.01050.x

Received May 2009; revised February 2010.
Address correspondence and reprint requests to Prof. M. Keith Sharp, Department of Mechanical Engineering, University of Louisville, 200 Sackett Hall, Louisville, KY 40292, USA. E-mail: keith.sharp@louisville.edu

increased as the external medium became more viscous. To simulate the deformation of cells in complex flows, many factors are involved, for instance, 3D fluid stresses applied to the membrane, the membrane's viscoelastic characteristics, interaction between cell membrane and flow, the membrane's tank-treading movements, and the membrane's time-dependent fatigue response. Pozrikidis (12) and Ramanujan and Pozrikidis (13) numerically simulated shear-induced deformation of a single cell modeled as a deformable liquid capsule enclosed by an elastic membrane resistant to shearing and bending. Numerical results for the period of rotation showed good agreement with experimental observations of Goldsmith and Marlow (14). While these studies have expanded our understanding of cell behavior in simple flows, the high concentration of cells in whole blood, as well as the complexity of cell deformation and membrane failure response constitute barriers to direct simulation of cells in suspension in cardiovascular flows. In the short term, continuum models for predicting hemolysis may be useful.

Simplified models include a curve fit by Sharp and Mohammad (15) to relate the critical shear stress τ_{sc} for hemolysis with exposure time t in hypodermic needles: $t(\tau_{sc}/1500 - 1)^2 = 0.01$. Heuser et al. (16) used a power law to estimate the fraction of plasma free hemoglobin from shear stress τ and t: $\Delta Hb/Hb = 1.8 \times 10^{-6}\, t^{0.765}\, \tau^{1.991}$. Giersiepen et al. (17) provided a similar model with different coefficients: $\Delta Hb/Hb = 3.62 \times 10^{-5}\, t^{0.785}\, \tau^{2.416}$. Being purely empirical, these models lack a logical connection to the deformation of cells under fluid stress, which is experimentally observable and which might be used for validation purposes. Because they do not include a mechanism of cell deformation to the point of lysis, it is challenging to incorporate new understanding about cell behavior into the models to improve them. In this article, a new hemolysis prediction model is developed that is based on a threshold of membrane strain. The model provides a foundation incorporating preliminary mechanics of membrane rupture that can be expanded as more insight is gained into the mechanisms of hemolysis in complex flows.

One necessary component of the new hemolysis prediction model was a model of membrane response in the ranges of membrane stress and strain that cause membrane failure. Hochmuth et al. (18) constructed a viscoelastic model for the cell membrane with experiments in which the cell was stretched with a micropipette and then released. Viscoelastic properties were inferred from the recovery of the cell to its unstressed shape. An improvement was added by Mohandas and Evans (19) that considered the membrane skeleton locally compressible. On the other hand, Rand (20) partially aspirated cells into a micropipette, with the remaining part of the cell forming a sphere outside the pipette, and measured the time required for the cell to be drawn completely into the bore. Membrane tension of 20–25 dyn/cm caused immediate membrane failure, though some cells ruptured at considerably lower stress. The range of exposure time to the resulting biaxial membrane tension was several to 200 s. Because these experiments exposed cells to stress and strain in the ranges relevant to at least partial membrane failure, Rand's model was used for the new hemolysis prediction model.

Another necessary component of the new model was a relationship between the flow field and cell membrane stress. A simplifying hypothesis, which also underlies the models of Heuser et al. (16) and Giersiepen et al. (17), was applied, which assumes that membrane stresses scale with continuum fluid stresses. This principle ignores the many types of flow-dependent cell motion and unifies the relationship between membrane and fluid stresses ad hoc for the empirical models, but implies a characteristic cell shape and orientation leading to membrane failure for a more mechanistic model. A prolate ellipsoidal shape was used based on images by Sutera and Mehrjardi (21).

Finally, hemolysis data from measured flow fields was necessary to validate the new model. Many experiments have demonstrated the relationship between viscous flow-induced hemolysis and both shear stress and exposure time (Table 1). For shorter exposure times (as short as 10^{-9} s [27,28]), lysis is caused by inertial forces. For shock wave flow with strength of 40 MPa, the inertial force was 910 dyn/cm^2, lasted for 3×10^{-9} s and caused area strain of about 10^{-5}, which induced transient pores that released hemoglobin (critical area strain of $10^{-7} \sim 10^{-5}$).

In previous observations of large shear-induced deformation of red cells, it was necessary to use a fixing agent (gluteraldehyde) to allow subsequent SEM imaging of the cells (21). In this project, a high-speed image capturing system was used to measure cell shape without the need for fixing chemicals, similar to the system of Zhao et al. (29), which was used to measure cell deformation in response to stress as high as 50 000 dyn/cm^2 and exposure time as short as 2 ms. Such observations at strains less than the hemolysis threshold can be used to calibrate a mechanistic model.

The amount of hemoglobin that escapes through the cell membrane, which is the desired result of any

TABLE 1. *Critical shear stress for different exposure times*

Exposure time: t (s)	Critical shear stress: τ_c (dyn/cm^2)	Geometry	Species	Reference
10^{-6}	10^5	Estimation	Human	Hellums and Hardwick (22)
10^{-5}	4×10^4	Turbulent jet	Human	Forstrom (23)
10^{-4}	5600	Oscillating wire	Human and canine	Williams et al. (24)
10^{-3}	4500	Oscillating bubble	Human and canine	Rooney (25)
10^2	1500	Concentric cylinder	Human	Leverett et al. (26)
2.4×10^2	2500	Concentric cylinder	Human	Sutera and Mehrjardi (21)

hemolysis prediction model, depends on the dynamics of membrane failure. Above Rand's (20) membrane area strain threshold of 6.4%, pores in the membrane may grow large enough to separate the cell into fragments, allowing all cell contents to escape, or if the cell is pulled into a dumbbell shape before failing, may release little hemoglobin. Alternatively, for brief exposure to high stress, pores may reseal before cell contents have escaped (1). Accounting for incomplete hemoglobin release during a membrane failure event is an important part of hemolysis prediction.

Previous developments toward mechanistic hemolysis prediction include that of Richardson (30), who used Jeffrey's (31) solution for the deformation of an ellipsoid in pure shear flow with Rand's (20) viscoelastic membrane model. A weakness of this model is that it may not apply to extensional flow, which is the other main component of general complex flows. Another weakness is that the model does not include the observed stress threshold below which membrane failure does not occur. Arora et al. (32) modeled cells as spherical liquid droplets that deform to ellipsoids with 40% excess surface area (the same as red cell membranes), plus an additional 6% area strain to begin hemoglobin release, which is taken to be proportional to the deformation of the ellipsoid beyond this limit. While this model provides a basis for calculating cell deformation and hemolysis in arbitrarily complex flows, it was calibrated to the hemolysis prediction of the Giersiepen et al. (17) model based on pure shear flow, which does not include a stress threshold. In this project, a simple control volume approach was used to relate membrane stress to arbitrary fluid stress that is exact for extensional flow, but not for high shear flow, for which the model may require some empiricism. This simple relationship offers the benefit of reduced computational time if the fit over a wide range of flows is acceptable. The model uses Rand's membrane model, with a stress threshold. To calibrate the model, images of moving cells deformed by a range of shear stresses were captured with a microscope-laser-camera system. The measured cell aspect ratios were compared with those predicted by the strain-based blood damage model to optimize the empirical coefficients in the model. This project represents the first step in verifying the model, which must also be tested in extensional and combined complex flows.

MATERIALS AND METHODS

An experimental system to create an observable, controlled flow under a microscope was constructed (33) (Fig. 1). The system comprised a flow subsystem, which consisted of a flow chamber, an upstream syringe pump (60 mL) and a downstream fluid reservoir, and an image capturing subsystem, which comprised a microscope, laser strobe, digital camera, and an image acquisition computer.

The chamber was designed to produce two-dimensional Poiseuille flow. The channel (0.4 mm wide, 2.4 mm deep, 40 mm long) was formed from two sheets of polymethyl methacrylate (PMMA),

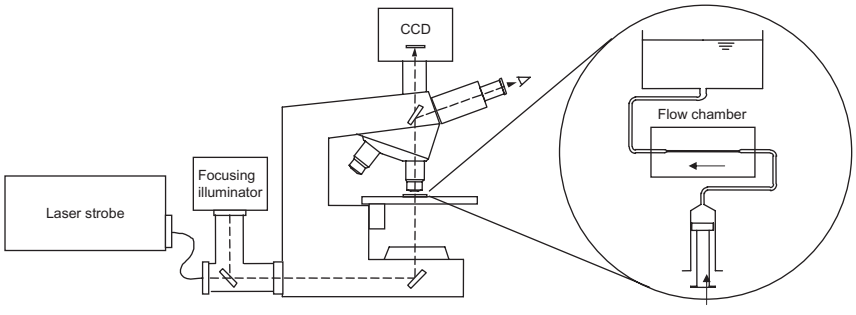

FIG. 1. Schematic of experimental system.

each micro-machined and then bonded together with acrylic cement. The depth of the channel, which was limited by the reach of the end mill, was chosen to be twice the working distance of the microscope objective for optical access to the middle depth of the channel. The channel width, which was the diameter of a readily available end mill, was approximately two orders of magnitude larger than a red cell. The total external thickness of the chamber was about 2.6 mm. Two 18-G stainless steel needles were connected to the chamber as inlet and outlet.

The pump, driven by a DC motor at 21.5 V, forced a dilute suspension of cells (23 mL volume per trial) through the flow channel. Positive pressure was applied to the channel to avoid vapor bubbles, which might be problematic for the microscope image and for estimating flow rate. A timer recorded the duration of each run so that volume flow rate could be calculated. Human blood samples, anticoagulated with citrate, were obtained from the American Red Cross and the University Hospital Blood Bank from seven different donors (S0-S6). For each experiment, performed at room temperature of about 24–25°C, 2 mL of blood was mixed with up to 200 mL of a solution of Dextran-500 in distilled water with 0.9% sodium chloride, with viscosity of 11.1 cP for all samples except S0, which was mixed to 8 cP. (Dextran has been shown to have an insignificant influence on red cell properties [34].) Fluid viscosity was measured by a Wells-Brookfield cone/plate viscometer. After each flow event, the solution for that run was discarded to ensure that cells were stressed only once. All seven blood samples from different donors were tested 24 days or less from collection, except for S0, which was outdated and was tested 42 days after collection. The flow was steady laminar, with average velocity of 3.2–3.9 m/s and Reynolds number *Re* of 100–200 (Fig. 2). For the largest *Re*, the calculated entrance length was 8 channel widths, which corresponds to 8% of the channel length. Wall shear stress τ_w was 4700–5600 dyn/cm^2 depending on the flow rate and fluid viscosity. The time required for a cell to travel along the whole channel at the mean flow velocity was about 10 ms. The field of view for the 16× objective was about 0.2 mm long and 0.15 mm wide, and was located 38 mm (95 channel widths) downstream of the entrance.

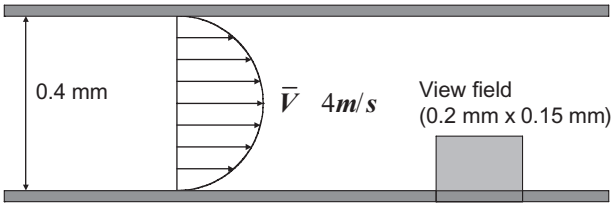

FIG. 2. 2D schematic diagram of the channel flow indicating the field of view.

An Nd-YAG laser with 3 ns pulse width and 20 μJ pulse energy at 543 nm wavelength was used to stop the motion of the flow. An optical fiber of 30 m length and 3 mm diameter reduced laser speckle. The laser light was expanded and collimated by two lenses at the exit of the optical fiber before entering the microscope.

The narrow depth of focus of the 16× long working distance microscope objective effectively isolated the plane of focus. A QImage QICAM-12 bit Fast 1394 digital camera (1/2 inch Sony ICX205 CCD, 1392×1040 array, 4.65 μm × 4.65 μm pixel size with 10 000 electron well depth, quantum efficiency of 40% at 543 nm, 12 bit resolution, 10 frames per second; QImaging, Surrey, BC, Canada) was mounted to the upper port of the Zeiss Photomicroscope II (Carl Zeiss, Inc., Thornwood, NY, USA) through a Diagnostic Instruments 1 × C-mount adapter tube (Diagnostic Instruments, Inc., Sterling Heights, MI, USA). A stage objective micrometer of 100 divisions/mm was used to calibrate length measurements in the images. To obtain images, a custom Labview program actuated a relay to start the pump, which provided about 7 s of flow. Then a signal was sent to QCapture Pro software, which first opened the camera shutter for 0.05 s per image, then pulsed the laser while the shutter was open and finally downloaded images 40 times at its maximum speed of about 0.15 s per frame.

The duration of exposure to shear was estimated for each cell by $t = l/v$ where l is the distance from the entrance to the location where the cell was observed and v is the velocity of the cell estimated by White (35)

$$\frac{v}{\bar{v}} = \frac{48}{\pi^3} \frac{\sum_{i=1,3,5\ldots} (-1)^{(i-1)/2} \left[1 - \frac{\cosh\left(\frac{i\pi y''}{2H}\right)}{\cosh\left(\frac{i\pi W}{2H}\right)} \right] i^{-3}}{1 - \frac{192H}{\pi^5 W} \sum_{i=1,3,5\ldots} \frac{\tanh\left(\frac{i\pi W}{2H}\right)}{i^5}} \quad (1)$$

where W is the half width of the channel, H is the half height of the channel, y'' is the distance of the cell's centroid from the center of the channel, and $\bar{v}$ is the mean flow velocity. The shear stress on the cell is found with a derivative of Eq. 1. The width to depth ratio of the channel caused the calculated shear to be about 11% higher than that between infinite plates.

The aspect ratio a/*b* of deformed cells was obtained by manually measuring major radius *a* and minor radius *b*.

HEMOLYSIS PREDICTION MODEL

The model has four major components: (i) a relationship between fluid stresses and cell membrane tension, (ii) a constitutive model relating membrane stress to strain, (iii) a strain threshold at which membrane rupture is predicted, and (iv) a model for the amount of hemoglobin released during the membrane failure event.

Fluid stress/membrane stress model

To simplify the representation of external flow, the deviatoric fluid stresses surrounding a single red cell were characterized by the local instantaneous values in a continuum by the three principal components [σ_1, σ_2, σ_3]. The non-uniform distribution of fluid stresses around the cell was ignored in this development. Dimensional analysis suggests that membrane stress *T*, cell orientation θ, motion ω, and shape *s* are dependent parameters that are determined by these fluid stresses τ, as well as other independent parameters related to unstressed cell dimensions *D* and membrane and cytoplasm properties ψ, where each parameter can have several components. In addition, since red cell membrane shear elasticity is approximately five orders of magnitude smaller than area elasticity, and bending elasticity is even smaller (36), it is recognized that deformation from the cell's unstressed biconcave disk shape to an elongated ellipsoidal shape will tend to occur with little membrane area change until further elongation requires an increase in membrane area to accommodate constant volume within the cell. Since membrane failure depends on the latter (area strain) stage of cell deformation, a threshold fluid stress τ_c is incorporated into the model, below which membrane area strain does not occur. The difference between the actual and threshold stresses is taken as the driving term for area strain and is represented as a single combined independent variable.

$$(T, \theta, \omega, s) = (T, \theta, \omega, s)(\tau - \tau_c, D, \psi) \quad (2)$$

The focus of this research is on *T*, the first of this set of relationships. For a design tool it is reasonable to assume average values of cell properties therefore *D* and Ψ can be ignored. The units of membrane stress *T* (force/length in this article) can be matched by fluid stress $(\tau - \tau_c)$ times a characteristic length *L*, which is chosen from among the set *s*, resulting in

$$T/[(\tau - \tau_c)L] = \text{constant} \quad (3)$$

L was characterized for extensional flow, which allows simple derivation of conservation equations, and results were compared with a numerical solution for shear flow.

To quantify the parametric relationship (3), it was assumed for conditions approaching membrane rupture that the cell would be stretched into a prolate ellipsoidal shape, similar to the spindle-like shape that has been observed in pure shear flow (10). Deforming the cell to the longest ellipsoidal shape that retains the same surface area and volume requires some initial externally applied stress τ_c that does not contribute to membrane area dilation. Beyond the isoarea limit, further elongation of the ellipsoid requires an increase in membrane surface area to contain constant volume of the cell. To estimate *L*, it was assumed that the major and two minor axes of the cell were aligned with the directions of the three principal stresses components. This cell orientation is exactly correct for extensional flow, and approximately correct for low shear flow (37), but the major axis has been shown to approach alignment with streamlines as shear increases (10). The same behavior was observed in the current experiments. However, because this approach provides the benefit of a relatively simple model, its evaluation for potential application to a wider range of complex flows was deemed worthwhile. A derivation based on shear flow would similarly require evaluation in extensional flow.

Using these assumptions, and a three-dimensional force balance on a control volume surrounding the cell (Appendix A), it can be found that Eq. 3 becomes

$$\hat{T} = \alpha \frac{4}{5} b(\tau_s - \tau_c) \quad (4)$$

where membrane tension is characterized by $T = \hat{T}$ and fluid stresses are characterized by the scalar stress $\tau = \tau_s$, $L = b$, and the constant is 4/5. In addition, τ_c can be determined explicitly in terms of membrane stretch ratios; however, in the calibration to follow, τ_c is used as an empirical parameter. Empirical constant α was introduced to account for approximations in the fluid stress/membrane relationship, for instance, the cyclical rather than steady stress in tank-treading membranes, non-ellipsoidal cell shapes, and cell orientation differing from the assumptions. The simplicity of this result, if validated, offers benefits in fast hemolysis prediction algorithms.

Because this relationship was derived for a cell alignment characteristic of extensional and low shear

flow, its universality for other types of flow, in particular high shear flow, should be evaluated. Therefore, membrane tension estimates from Eq. 6 were compared with theoretical estimates for high shear flow. Tran-Son-Tay et al. (38) calculated membrane tension based on a model by Keller and Skalak (39) of steady viscous internal and external flow around an ellipsoidal Kelvin–Voigt viscoelastic cell membrane with negligible area deformation and prescribed shape, orientation, and tank-treading velocity distribution. Their equations (which, in the interest of brevity, are not repeated here) were applied to the cell measurements obtained during this investigation. Data used as inputs to the equations were the shear rate, external fluid viscosity, long axis angle, and long axis and one short axis radii measured for each red cell image. The second (cross-stream) short axis radius was not measurable from the images, so was estimated. As Tran-Son-Tay et al. note, the approximations inherent in the model lead to non-uniform estimates of pressure within the cell. While they used the average of the pressures estimated at the downstream tip (their "location I") and at the midpoint (location II) to determine membrane stresses, the latter pressure estimate was unstable for the much higher shear rates of our experiments.

Membrane constitutive relationship

Membrane area response was assumed to be viscoelastic with biaxial tension $\hat{T}$ related to area strain S and time t (20)

$$\frac{1}{\hat{T}} = \frac{1}{ShY_2} + \frac{1}{ShY_1}\left(1 - \exp\frac{-Y_1}{\eta_1}\right) + \frac{t}{Sh\eta_2} \qquad (5)$$

where h is the membrane thickness, Y_1 and Y_2 are Young's moduli, and η_1 and η_2 are viscosities. This equation represents a Maxwell–Voigt model of membrane area response, in which the Voigt component—spring Y_1 and parallel dash-pot η_1—is related to short-term strain, and the Maxwell component—spring Y_2 in series with dash-pot η_2—is related to long time response.

Rand (20) found $Y_1 \sim 4.3 \times 10^8$ dyn/cm^2, $Y_2 \sim 4.8 \times 10^8$ dyn/cm^2, $\eta_1 \sim 5.3 \times 10^7$ dyn·s/cm^2, and $\eta_2 \sim 1.1 \times 10^{11}$ dyn·s/cm^2 for an estimated membrane thickness of $h \sim 10^{-6}$ cm, thus $h\eta_1 \sim 53$ dyn·s/cm and $h\eta_2 \sim 1.1 \times 10^5$ dyn·s/cm. Evans and Hochmuth (40) and Hochmuth et al. (18), however, found the viscosity of the membrane surface to be $\eta_m = (6 \pm 2) \times 10^{-4}$ dyn·s/cm, about five and eight orders of magnitude smaller than $h\eta_1$ and $h\eta_2$, respectively, and concluded that viscous flow in the membrane could not be responsible for the temporal dependence of membrane response in Rand's experiments.

The reason for the large differences in the viscosities interpreted from the two sets of experiments may lie in the comparison of the protocols. In Rand's experiments, a micropipette was used to aspirate part of the red cell into the bore, with the other part of the cell remaining outside the bore forming a sphere. The exposure time until the cell disappeared into the bore of the micropipette was recorded. In Evans and Hochmuth's experiments (40), the cell was pulled in opposition by two micropipettes and then released. Cell dimensions and recovery time were measured as the cell returned to its biconcave shape. The recovery may involve two components, depending on the magnitude of the initial deformation. Recovery from small deformation may involve no membrane area strain. For larger deformation, recovery also involves a return to unstressed membrane area, with this component being characterized by different elastic and viscous coefficients. Sutera and Mehrjardi (21) observed that cells began to lose their biconcavity at a stress of around 500 dyn/cm^2, and a majority of them became prolate ellipsoidal when the stress exceeded about 1500 dyn/cm^2 for an exposure time of 4 min. These fluid stress levels are associated with the range of membrane tension for which cells are deformed without area strain. The order of the involved membrane tension is estimated by $T \sim \tau \cdot a$, where T is membrane tension, τ is shear stress, and a is major radius. Taking $\tau \sim 500$ dyn/cm^2 and $a \sim 4$ μm, T required to cause area strain is higher than about 0.2 dyn/cm. The recovery times t_c measured in the Evans and Hochmuth experiments were about 0.1 s. Therefore, the viscous component of membrane tension in their experiments were of order $\eta_m/t_c = 6 \times 10^{-4}/0.1 = 6 \times 10^{-3}$ dyn/cm, which is much smaller than the membrane tension needed to cause, or to resist recovery from, area strain during the recovery period. Therefore, the viscosity in their experiments was actually related to isoarea deformation, and not to the area expansion required to produce lysis.

Y_1 and Y_2 in Rand's (20) model were verified by Evans et al. (41), who found isotropic tension proportional to area expansion $\hat{T} = K\frac{\Delta A}{A}$, where ΔA is the increase in surface area, A the original area, and K the area expansion modulus. At room temperature, the value of K was 450 dyn/cm ± 15 (42). Converting to stress units with $hY_2 = K$ gives $Y_2 = 4.5 \times 10^8$ dyn/cm^2. Rand's $Y_1 \sim 4.3 \times 10^8$ dyn/cm^2 and $Y_2 \sim 4.8 \times 10^8$ dyn/cm^2 were comparable with each other and to the Waugh and Evans value.

Hemolysis prediction threshold

An area strain threshold for cell lysis $S_c = 0.064$ (20,43) was adopted. Equation 5 can be normalized by S_c

$$\frac{S}{S_c} = \hat{T}\left[\frac{1}{S_c h Y_2} + \frac{1}{S_c h Y_1}\left(1 - \exp\frac{-Y_1}{\eta_1}t\right) + \frac{t}{S_c h \eta_2}\right] \quad (6)$$

Combining Eqs. 4 and 6 and reducing to a form for fitting experimental results

$$\frac{S}{S_c} = \frac{4\alpha b}{5}(\tau_s - \tau_c)[C_0 + C_1(1 - \exp(-C_2 \cdot t)) + C_3 \cdot t] \quad (7)$$

where $C_0 = \frac{1}{S_c h Y_2} = 3.5 \times 10^{-2}$ cm/dyn, $C_1 = \frac{1}{S_c h Y_1} = 3.9 \times 10^{-2}$ cm/dyn, and $C_3 = \frac{1}{S_c h \eta_2} = 1.5 \times 10^{-4}$ cm/dyn s (20). $\tau_c = 1500$ dyn/cm^2 was adopted based on observations by Sutera and Mehrjardi (21), and the hemolysis threshold of Sharp and Mohammad (15). While $C_2 = \frac{Y_1}{\eta_1} = 8\ \text{sec}^{-1}$ from Rand (20), α and C_2 were used as curve fit parameters, and represent the two empirical terms in the model.

Model of incomplete hemoglobin release

This part of the hemolysis prediction model, which is not included in Eq. 7, cannot be calibrated with the experiments described in this article, thus it will be left for a subsequent report. It is mentioned here for completeness, and as a reminder that this factor is critical to accurate predictions.

Calibration of the model with images of deformed cells

S was predicted with Eq. 7 from measured τ_s, t, and b for each cell, which was assumed to maintain a prolate ellipsoidal shape with volume and surface area

$$V = \frac{4}{3}\pi a b^2 \quad (8)$$

$$A = 2\pi\left[b^2 + \frac{a^2 b}{\sqrt{a^2 - b^2}}\arcsin\sqrt{1 - \frac{b^2}{a^2}}\right] \quad (9)$$

For mean cell volume $V = 96\ \mu m^3$ and unstressed surface area $A_0 = 130\ \mu m^2$ at 300 mosmol (44), unstressed aspect ratio $a/b = 3.85$ can be found by iteration from Eqs. 8 and 9. For a cell experiencing strain, the stressed aspect ratio can be found similarly where the surface area A of the strained cell is given by

$$\frac{A}{A_0} = 1 + S$$

For $S_c = 0.064$, aspect ratio becomes 4.76, corresponding to $a = 8.1\ \mu m$ and $b = 1.7\ \mu m$ for Fung's average cell. For convenience, the relationship between aspect ratio and strain was curve fit $a/b = 14.17(S + 1) - 10.33$ with good accuracy $R^2 = 0.9998$.

Erythrocyte volume and surface area exhibit Gaussian distributions within a sample of blood (44) and may vary among individuals. Moreover, cell dimensions depend on tonicity (osmolarity) (44). For instance, at 217 mosmol, mean volume increases to 116 μm^3 and mean surface area to 135 μm^2. These differences, which were found to be significant in the blood samples used for these experiments, influence the relationship between aspect ratio and area strain for each cell. Because the experimental protocol did not provide a convenient way to measure unstressed dimensions of the particular cells for which images were captured, this problem was addressed by reducing the set of images analyzed to those of a narrow range of sphericity, defined as the actual surface area of the cell divided by the surface area of a sphere of the same volume

$$Sph = \frac{4\pi}{(4\pi/3)^{2/3}} \cdot \frac{V^{2/3}}{A} \quad (10)$$

For Fung's (44) average cell at 300 mosmol, $Sph = 0.79$. Cells with similar Sph have similar relationships between a/b and S. Unstressed Sph was estimating for each cell image, and images within one standard deviation of the average Sph were analyzed. For example for subject S0, the estimated average Sph of red cells was 0.85 with standard deviation of about 0.03, thus images within the range $0.82 < Sph < 0.88$ were kept. The coefficients for the mean Sph in the relationship between a/b and S were applied to the whole reduced data set for this subject. A macro Visual Basic program was written to perform multiple regression to obtain values of α and C_2 that minimized the sum of squared differences between predicted and measured a/b.

Error propagation

Channel measurement uncertainty was 0.0254 mm (with the nondimensional uncertainty in channel width being the largest of all measured variables at 6.35%), total volume of the flow event 0.1 mm^3, duration of flow 0.01 s, fluid viscosity 0.1 cP, and cell

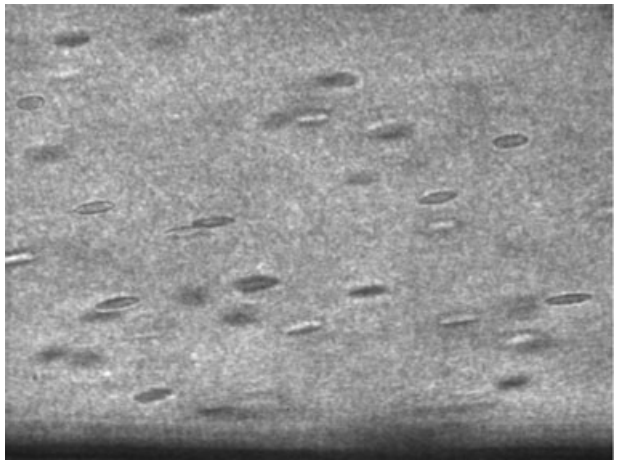

FIG. 3. Example image of moving cells (for field of view shown in Fig. 2). Direction of flow left to right.

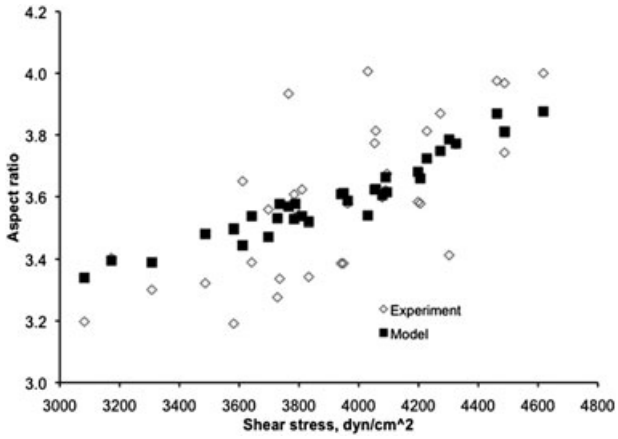

FIG. 4. Comparison of predicted and measured aspect ratio versus shear stress with two optimized parameter values fit to cell image data. Coefficient of determination $R^2 = 0.499$ for the experimental points.

dimensions and distance from the wall 0.1 μm. From these uncertainties in measured variables, estimated uncertainty of cell aspect ratio was 2.62%, exposure time 9.05%, and shear stress 11.1%.

RESULTS

An example image is shown in Fig. 3. Cells in the focal plane of the objective lens, identifiable by high contrast boundaries, were measured. Fragmented cells, identified as those with abnormally small cross sectional areas, were ignored.

Specifications for the seven blood samples are shown in Table 2. The number of frames chosen with clear cell images and number of cells measured are listed. Comparisons between predicted and measured a/*b* for all subjects are shown in Figs. 4 and 5 for regression parameter values $\alpha = 39.01$ and $C_2 = 84\ s^{-1}$, $R^2 = 0.407$.

The angle of attack of the cells (see, for instance, Fig. 3) was 4.88 ± 0.85 degrees, and are consistent with previous findings for shear flow (45). These angles, along with measured a and *b*, and estimate $c = 1.055\ b$, which provided a match of mean membrane stresses between the two groups, were used to calculate membrane stress by the Tran-Son-Tay et al. (38) method. Similar slopes of membrane stress versus fluid shear stress were obtained between the two models (Fig. 6).

The hemolytic fluid stress for the strain-based model (Eq. 7 with $S/S_c = 1$) fits experimental hemolysis threshold data (15) reasonably well, except for exposure time less than about 0.1 ms (Fig. 7). Even for a threshold of 100% hemolysis, the Giersiepen et al. (17) model overpredicts hemolysis for all exposure times. The Heuser et al. (16) model is closer, but both power-law models have slopes that decrease too rapidly with increasing exposure time to permit good fits. The time-linear term of Richardson (30) model, $t\tau_s^2 = 670$, has an even steeper slope. The empirical Sharp and Mohammad (15) model, $t\,(\tau_s/1500 - 1)^2 = 0.01$ exhibits the most suitable shape of curve to fit a wide range of exposure times.

DISCUSSION

The laser-illuminated micro imaging technique provides an effective, noninvasive method to capture

TABLE 2. *Experimental specifications*

Subject	Duration* (days)	Number of cell images	Fluid viscosity (cP)	Average velocity (m/s)	Field of view location (mm)	Number of frames
S0	>42	50	8.0	3.93	37.59	43
S1	24	83	11.1	3.38	36.26	65
S2	19	113	11.1	3.28	36.26	74
S3	18	88	11.1	3.27	36.26	57
S4	17	55	11.1	3.18	36.26	45
S5	17	91	11.1	3.25	36.26	60
S6	17	102	11.1	3.22	36.26	69

* Time from collection date to date of experiment, in days.

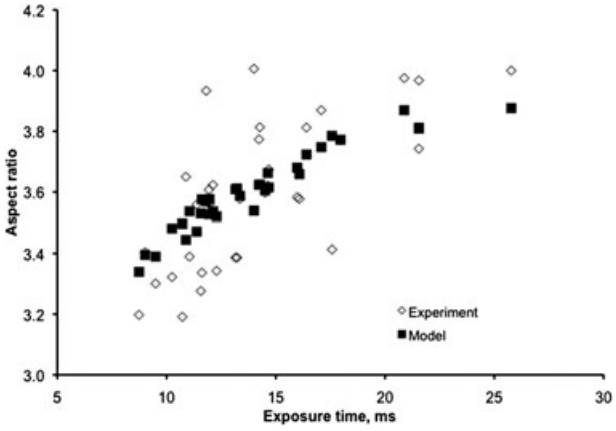

FIG. 5. Comparison of predicted and measured aspect ratio versus exposure time with two optimized parameter values fit to cell image data. Coefficient of determination $R^2 = 0.476$ for the experimental points.

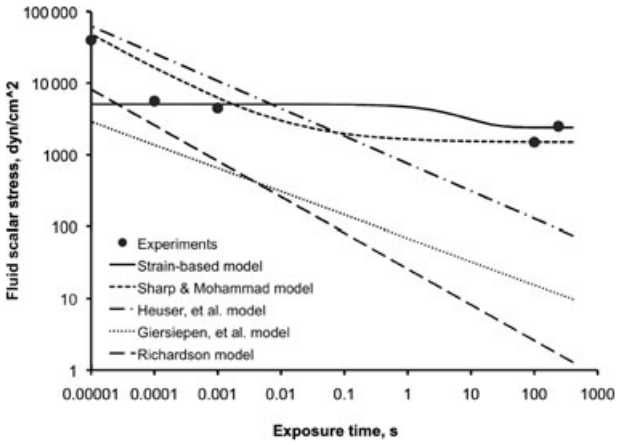

FIG. 7. Comparison of hemolysis threshold models to data. (100% hemolysis was used for Heuser et al. and Giersiepen et al. models).

and investigate the deformation of cells by fluid stresses in high-speed flows. The strain-based blood damage model provides an estimate of flow-induced membrane area strain, which facilitates comparison of model predictions with experimental observations. In this study, analyses of the images of deformed cells were used to validate and optimize the coefficients of the strain-based blood damage model.

Figures 4 and 5 show good fits of predicted to measured cell aspect ratio considering that the predictions are based on constant sphericity, while the range of sphericity of the measured cells contributes considerable scatter to the actual cell aspect ratio. Because aspect ratio is sensitive to sphericity, correlation might be improved if aspect ratio could be calculated for the individual sphericity of each cell. However, measurements that would allow such calculations were not possible with this experimental set up.

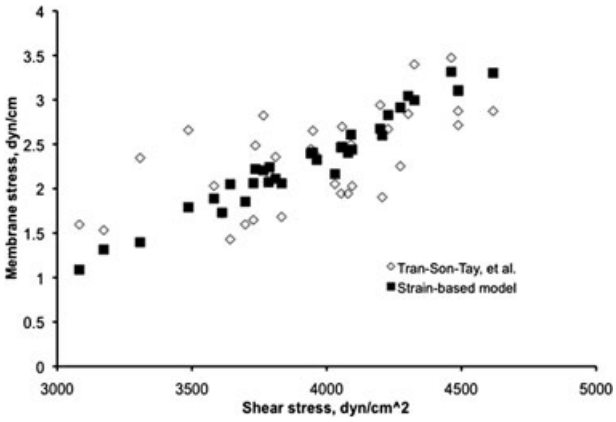

FIG. 6. Comparison of membrane stress predicted by the Tran-Son-Tay et al. model and by Eq. 4.

The empirically derived value of $C_2 = 84\ s^{-1}$, which influenced the slope of a/*b* versus stress and exposure time, provides an estimate of viscous term $h\eta_1 = hY_1/C_2 = 5.12$ dyn·s/cm, which is an order of magnitude smaller than Rand's (20) value $h\eta_1 = 53$ dyn·s/cm, and five orders of magnitude larger than Hochmuth et al. (18) $\eta_1 = (6 \pm 2) \times 10^{-4}$ dyn·s/cm, which was related to deformation without area strain. C_3 is only related to long exposure time, and was an insignificant term for these experiments.

τ_c has a relatively small influence on the magnitude and slope of predicted a/*b* versus stress or exposure time. $\tau_c = 1500$ dyn/cm^2 perhaps seems high compared with the experiments of Sutera and Mehrjardi (21), in which cells were observed to assume a prolate ellipsoidal shape within 4 min for shear stress as low as 500 dyn/cm^2. However, it should be noted that the current experiments had much shorter exposure times. If the trend of higher hemolysis stress for shorter exposure also applies for τ_c, then τ_c may be large for the short exposure times (~0.01 s) of these experiments, but smaller for the longer exposure times (~100 s) characteristic of the Sutera and Mehrjardi images. Revision of the model to account for duration dependent τ_c may improve the range of stress over which the model applies. The model also does not address the effects of repeated exposure, that is, damage accumulation (see, for instance, Yeleswarapu et al. [46]).

The current strain-based model does not fit well for very short exposure times ($t \leq 0.1$ ms, Fig. 7). Recall that Rand's cell membrane model included only

springs and dash-pots. For such short times, a mass term might be necessary and significant. Similarly, the inertial term that was neglected in the momentum conservation equations relating membrane tension to fluid stresses may become important for short exposures, as might a viscous term associated with the deformation of the cytoplasm.

The success of the model hinges on its applicability to a wide range of flows. Since the force balances for the model were developed for a simplified cell orientation that is most characteristic of extensional flow, validation for a range of orientations produced by different flows is key. A partial test of the potential universality of the model is provided by comparison with the Tran-Son-Tay et al. (38) model for the limit of cells in pure shear flow. However, because membrane stress calculated by the Tran-Son-Tay et al. method is sensitive to c, which was not available from the images, the apparent agreement should be viewed with caution. Nonetheless, the estimate of c that produces good agreement is within reason and therefore does not disprove the model.

Comparison of the new strain-based model with that of Richardson (30) also provides insight into the advantages and disadvantages of each. The Richardson model has exposure time inversely proportional to the square of fluid stress, which provides a better fit to the experimental points in Fig. 7 for very short exposure time. This difference may be indicative of the lack of dependence in the new model on the reduced angle of attack of the cell with increasing shear, which increases the threshold stress for hemolysis. On the other hand, the inclusion of an isoarea threshold stress greatly improves the performance of the new model at long exposure time relative to the Richardson model.

The empirical models of Heuser et al. (16) and Giersiepen et al. (17) might also provide improved predictions for long exposure times by inclusion of a threshold stress. Though a curve for the deformation-based hemolysis prediction of Arora et al. (32) is not plotted in Fig. 7, it could be expected, because they calibrated their model to the Giersiepen et al. power law, to follow the Giersiepen et al. curve in Fig. 7 and perhaps to similarly benefit from incorporation of an isoarea threshold stress.

CONCLUSION

Since the strain-based blood damage model provides reasonable estimates of shear-induced deformation of red cells for exposure times typical of many cardiovascular flows, the suitability of the model for predicting membrane failure based on a threshold of membrane area strain will be tested in future studies of more complex flows. This model has the potential to reduce the empiricism of hemolysis prediction.

Acknowledgments: The authors acknowledge support from the Kentucky Science and Engineering Foundation, donation of red blood samples from the American Red Cross-River Valley Region in Louisville, KY, USA and from the University of Louisville Hospital Blood Bank, assistance of Scott Cambron in machining the flow channel, Robert Keynton for loan of a camera for preliminary experiments, George Pantalos for loan of the syringe pump, and Roger Tran-Son-Tay for advice regarding his simulations.

APPENDIX

Hypothesized deformation patterns for the cells experiencing three-dimensional stresses include oblate and prolate ellipsoids and spheres (33). The prolate ellipsoid, which would tend to occur when there is one dominant positive principal stress, may be the most common condition in cardiovascular flows. Even though the prolate ellipsoid ostensibly requires $b \approx c$ and $\sigma_2 \approx \sigma_3$, similar shapes have been observed in pure shear flow, for which $\sigma_2 = 0$ and $\sigma_3 \approx -\sigma_1$. Therefore, the approximately prolate ellipsoidal shape may occur for a wide range of hemolytic stress conditions and, accordingly, was assumed in the quantification of Eq. 4.

To estimate L and the constant in Eq. 4, dynamic force equilibrium was applied to half a prolate ellipsoidal cell in the x direction (Fig. A1). T_1 is the average membrane tension on the circumference of the cell, Δp is the pressure difference between internal and external fluids. $A_1 = \pi b^2$ is the cross-sectional area, and $L_1 = 2\pi b$ is the circumference. Acceleration $[\dot{v}_1, \dot{v}_2, \dot{v}_3]$ is defined in the three principal directions.

For the half cell, conservation of linear momentum in direction x leads to

$$T_1 = (\sigma_1 + \Delta p)\frac{A_1}{L_1} - \frac{m\dot{v}_1}{2L_1} \qquad \text{(A1)}$$

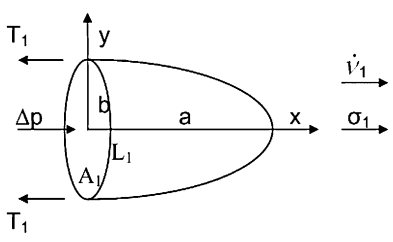

FIG. A1. Free body diagram of the forces acting on the half cell in the x direction.

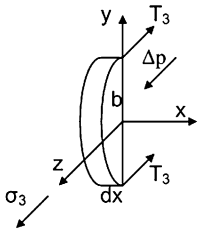

FIG. A2. Free body diagram for force equilibrium in the z direction.

where m is the mass of the half cell.

A criterion for neglecting the inertial term can be found with T_1 estimated from the critical membrane tension T_c of around 0.01 N/m, $m \sim 10^{-10}$ kg and $L_1 \sim 20\ \mu$m, which gives $\dot{v}_1 \ll \frac{2T_1L_1}{m} \sim 4\times10^6\ \mathrm{m/s^2}$. The maximum acceleration in physiologic cardiovascular flows is limited by the available pressure difference across the heart of about 200 mm Hg. The maximum acceleration for inviscid flow, $\dot{v}_{\max} \approx \frac{1}{\rho}\frac{\Delta P}{\Delta x} = 27\,000\ \mathrm{m/s^2}$, where $\Delta \boldsymbol{x}$ is estimated as 1 mm, satisfies the above condition. In the flow channel used for these experiments, the pressure difference is limited to the vapor pressure of water. Estimating $\Delta \boldsymbol{x}$ as one entrance length, the characteristic maximum acceleration becomes $v_{\max} \approx 21\,000$ m/s^2, which is also well below the threshold. Acceleration may be higher locally in the entrance and other nonphysiologic and externally driven flows, such as shock wave flow (1), may produce higher acceleration, but will be neglected in this initial development. Without the acceleration term, Eq. A1 becomes

$$T_1 = (\sigma_1 + \Delta p)\frac{A_1}{L_1} = (\sigma_1 + \Delta p)\frac{\pi b^2}{2\pi b} = (\sigma_1 + \Delta p)\frac{b}{2} \quad \text{(A2)}$$

To analyze equilibrium in the z directions, half of a differential slice dx was taken from the elongated cell (Fig. A2). The free body diagram for equilibrium in the y direction is similar. The balance of forces about the differential element give

$$T_2 = (\sigma_2 + \Delta p)\,b \text{ and } T_3 = (\sigma_3 + \Delta p)\,b \quad \text{(A3)}$$

Defining $\xi_2 = \frac{T_2}{T_1}$ and $\xi_3 = \frac{T_3}{T_1}$, and combining Eqs. A2 and A3 to eliminate Δp, gives

$$\frac{2T_1 - T_2}{b} = T_1\frac{2-\xi_2}{b} = \sigma_1 - \sigma_2 \quad \text{and}$$
$$\frac{2T_1 - T_3}{b} = T_1\frac{2-\xi_3}{b} = \sigma_1 - \sigma_3 \quad \text{(A4)}$$

The two average membrane tensions are defined as

$$\bar{T}_2 = \frac{T_1 + T_2}{2} \quad \text{and} \quad \bar{T}_3 = \frac{T_1 + T_3}{2} \quad \text{(A5)}$$

which by inserting Eq. A4 can be expressed as

$$\bar{T}_2 = \frac{1+\xi_2}{2-\xi_2}\frac{b}{2}(\sigma_1 - \sigma_2) \quad \text{and}$$
$$\bar{T}_3 = \frac{1+\xi_3}{2-\xi_3}\frac{b}{2}(\sigma_1 - \sigma_3) \quad \text{(A6)}$$

This part of the model can now be closed with estimate $\xi = \xi_2 = \xi_3 \approx \frac{1}{3}$ (13), which provides two estimates of mean membrane tension

$$\bar{T}_2 = \frac{2b}{5}(\sigma_1 - \sigma_2) \quad \text{and} \quad \bar{T}_3 = \frac{2b}{5}(\sigma_1 - \sigma_3) \quad \text{(A7)}$$

Because $\sigma_1 \geq \sigma_2 \geq \sigma_3$ by convention, the second of Eq. A7 provides the largest mean membrane stress and therefore the more conservative relationship for predicting hemolysis. Throughout the rest of the article, mean membrane stress will be taken as its maximum value $\bar{T} = \bar{T}_3$.

The biaxial membrane tension causing area dilation has been modeled with a viscoelastic relationship (18,40). Using the notation in the previous paragraph for the maximum mean stress

$$\hat{T} = \bar{T}_3 - \mu_m\frac{(\lambda_1 - \lambda_3)^2}{4} \quad \text{(A8)}$$

where $\hat{T}$ is the biaxial tension causing area dilation of a cell surface, λ_1 and λ_3 are the principal extension ratios, and μ_m is the shear modulus. The shear term can be replaced with a threshold fluid stress difference $\tau_c \equiv \frac{5\mu_m}{b}\frac{(\lambda_1 - \lambda_3)^2}{16}$ required to deform the cell to its isoarea ellipsoidal shape. Inserting the maximum stress from Eq. A7 gives

$$\hat{T} = \frac{2b}{5}(\sigma_1 - \sigma_3 - 2\tau_c) \quad \text{(A9)}$$

The scalar stress τ_s used in previous literature (47) to model hemolysis is proportional to the von Mises stress. For pure shear flow, $\tau_c = \tau_{vM}/\sqrt{3} = \frac{\sigma_1 - \sigma_3}{2}$, where τ_{vM} is the von Mises stress, thus Eq. A8 becomes

$$\hat{T} = \frac{4b}{5}(\tau_s - \tau_c) \quad \text{(A10)}$$

REFERENCES

1. Lokhandwalla M, Sturtevant B. Mechanical hemolysis in shock wave lithotripsy (SWL): I. Analysis of cell deformation due to SWL flow fields. *Phys Med Biol* 2001;46:413–37.
2. Raisky F, Gauthier C, Marchal A, Blum D. Haemolyzed samples responsibility of short catheters. *Ann Biol Clin Paris* 1994;52:523–7.
3. Kawahito K, Nosé Y. Hemolysis in different centrifugal pumps. *Artif Organs* 1997;21:323–6.
4. Luckras H, Woods M, Large SR. And hemlysis goes on: ventricular assist device in combination with veno-venous hemofiltration. *Ann Thorac Surg* 2002;73:546–8.
5. Tsuji A, Tanabe M, Onishi K, et al. Intravascular hemolysis in aortic stenosis. *Intern Med* 2004;43:935–8.
6. Vavuranakis M, Tzannos KA, Thanopoulos BD, Vlasis K, Stefanadis C. Severe hemolysis complicating transcatheter occlusion of a patent ductus arteriosus: the importance of elimination of residual flow. *Hellenic J Cardiol* 2007;48:373–6.
7. Anil SR, Sivakumar K, Philip AK, Francis E, Kumar RK. Clinical course and management strategies for hemolysis after transcatheter closure of patent ductus arteriosus. *Catheter Cardiovasc Interv* 2003;59:538–43.
8. Dhaene M, Gulbis B, Lietaer N, et al. Red blood cell destruction in single-needle dialysis. *Clin Nephrol* 1989;31:327–31.
9. Fischer TM, Stohr-Liesen M, Schmid-Schonbein H. The red cell as a fluid droplet: tank tread-like motion of the human erythrocyte membrane in shear flow. *Science* 1978;202:894–6.
10. Secomb TW. Mechanics of red blood cells and blood flow in narrow tubes. In: Pozrikidis C, ed. *Modeling and Simulation of Capsules and Biological Cells*. Chapter 4. London: Chapman & Hall/CRC, 2003;168–9.
11. Pfafferott C, Nash GB, Meiselman HJ. Red blood cell deformation in shear flow: effects of internal and external phase viscosity and of in vivo aging. *Biophys J* 1985;47:695–704.
12. Pozrikidis C. Numerical simuation of the flow-induced deformation of red blood cells. *Ann Biomed Eng* 2003;31:1194–205.
13. Ramanujan S, Pozrikidis C. Deformation of liquid capsules enclosed by elastic membranes in simple shear flow: large deformations and the effect of fluid viscosities. *J Fluid Mech* 1998;361:117–43.
14. Goldsmith HL, Marlow J. Flow behaviour of erythrocytes. I. Rotation and deformation in dilute suspensions. *Proc R Soc Lond Ser B* 1972;182:351–84.
15. Sharp MK, Mohammad SF. The scaling of hemolysis in needles and catheters. *Ann Biomed Eng* 1998;26:788–97.
16. Heuser G, Opitz RA. Couette viscometer for short time shearing in blood. *Biorheology* 1980;17:17–24.
17. Giersiepen M, Wurzinger LJ, Opitz R, Reul H. Estimation of shear stress-related blood damage in heart valve prostheses: in vitro comparison of 25 aortic valves. *Int J Artif Organs* 1990;13:300–6.
18. Hochmuth RM, Worthy PR, Evans EA. Red cell extensional recovery and the determination of membrane viscosity. *Biophys J* 1979;26:101–14.
19. Mohandas N, Evans EA. Mechanical properties of the red cell membrane in relation to molecular structure and genetic defects. *Ann Rev Biophys Biomol Struct* 1994;23:787–818.
20. Rand RP. Mechanical properties of the red cell membrane: II. Viscoelastic breakdown of the membrane. *Biophys J* 1964;4:303–16.
21. Sutera SP, Mehrjardi MH. Deformation and fragmentation of human red blood cells in turbulent shear flow. *Biophys J* 1975;15:1–10.
22. Hellums JD, Hardwick PA. Response of platelets to shear stress—a review. In: Gross DR, Hwang NHC, eds. *The Rheology of Blood, Blood Vessels and Associated Tissue*. Rockville: Sijthoff & Noordhoff, 1981;160.
23. Forstrom RJ. A new measure of erythrocyte membrane strength: the jet fragility test. PhD thesis, University of Minnesota, Minneapolis, 1969.
24. Williams AR, Hughes DE, Hyborg WL. Hemolysis near a transversely oscillating wire. *Science* 1970;169:871–3.
25. Rooney JA. Hemolysis near an ultrasonically pulsating gas bubble. *Science* 1970;169:869–71.
26. Leverett LB, Hellums JD, Alfrey CP, Lynch EC. Red blood cell damage by shear stress. *Biophys J* 1972;12:257–73.
27. Williams JC, Woodward JF, Stonehill MA, Evans AP, McAteer JA. Cell damage by lithotripter shock waves at high pressure to preclude cavitation. *Ultrasound Med Biol* 1999;25:1445–9.
28. Lokhandwalla M. Damage mechanism in shock wave lithotripsy. PhD Thesis, California Institute of Technology, Pasadena, CA, 2001.
29. Zhao R, Antaki JF, Naik T, Bachman TN, Kameneva MV, Wu ZJ. Microscopic investigation of erythrocyte deformation dynamics. *Biorheology* 2006;43:747–65.
30. Richardson E. Applications of a theoretical model for haemolysis in shear flow. *Biorheology* 1975;12:27–37.
31. Jeffrey GB. The motion of ellipsoidal particles immersed in a viscous fluid. *Proc R Soc Lond* 1922;A102:161–79.
32. Arora D, Behr M, Pasquali M. A tensor-based measure for estimating blood damage. *Artif Organs* 2004;28:1002–15.
33. Chen Y. Analysis and experiments on flow-induced hemolysis. PhD thesis, Department of Mechanical Engineering, University of Louisville, 2006.
34. Tran-Son-Tay R, Nash GB, Meiselman HJ. Effects of dextran and membrane shear rate on red cell membrane viscosity. *Biorheology* 1985;22:335–40.
35. White FM. *Viscous Fluid Flow*. New York: McGraw-Hill, 1991.
36. Hochmuth RM. Properties of red blood cells. In: Skalak R, Chien S, eds. *Handbook of Bioengineering*. Chapter 12. New York: McGraw-Hill, 1987;12.1–12.17.
37. Zhao Y, Sharp MK. Finite element analysis of the lift on a slightly deformable and freely rotating and translating circular cylinder in two-dimensional channel flow. *J Biomech Eng* 1999;121:148–52.
38. Tran-Son-Tay R, Sutera SP, Zahalak GI, Rao PR. Membrane stress and internal pressure in a red blood cell freely suspended in a shear flow. *Biophys J* 1987;51:915–24.
39. Keller SR, Skalak R. Motion of a tank-treading ellipsoidal particle in a shear flow. *J Fluid Mech* 1982;120:27–47.
40. Evans EA, Hochmuth RM. Membrane viscoelasticity. *Biophys J* 1976;16:1–10.
41. Evans EA, Waugh R, Melnik L. Elastic area compressibility modulus of red cell membrane. *Biophys J* 1976;16:585–95.
42. Waugh RE, Evans EA. Thermoelasticity of red blood cell membrane. *Biophys J* 1979;26:115–32.
43. Blackshear PL, Blackshear GL. Mechanical hemolysis. In: Skalak R, Chien S, eds. *Handbook of Bioengineering*. Chapter 15. New York: McGraw-Hill, 1987;15.1–9.
44. Fung YC. *Biomechanics: Mechanical Properties of Living Tissues*, 2nd Edition. New York: Springer-Verlag, 1993;116.
45. Fischer TM. On the energy dissipation in a tank-treading human red blood cell. *Biophys J* 1980;32:863–8.
46. Yeleswarapu KK, Antaki JF, Kameneva MV, Rajagopal KR. A mathematical model for shear-induced hemolysis. *Artif Organs* 1995;19:576–82.
47. Bludszuweit C. Model for a general mechanical blood damage prediction. *Artif Organs* 1995;19:583–9.